A Rapid Thermal-Radiation-Assisted Sintering Strategy for Nd–Fe–B-Type Magnets

Tomaž Tomše,* Aljaž Ivekovič, Andraž Kocjan, Sašo Šturm, and Kristina Žužek

The green transition has spiked demand for high-performance sintered Nd–Fe–B permanent magnets, necessitating advanced powder consolidation technologies to enhance production efficiency. This study explores the rapid sintering methodology for an Nd–Fe–B powder using a radiation-assisted sintering approach. The case study material is an industrially used powder, prepared through strip-casting, hydrogen decrepitation, and jet milling, with a mean particle size of 5.5 μm. The powder is sintered to full density in a modified spark plasma sintering furnace, achieving pressureless conditions and eliminating electrical currents in the sample to preserve grain alignment and prevent decomposition of the hard-magnetic phase. Fully dense samples are obtained with heating rates ranging from 10 to 200 °C min^{-1} and up to 5 min of dwell time at 1100 °C. Rapid heating results in grain size and microstructure comparable to conventionally sintered magnets prepared from the same powder, without compromising magnetic performance after postsinter annealing at 520 °C for 120 min. This sintering method contributes to a novel strategy for optimizing magnet production by utilizing efficient thermal-radiation heat transfer. The combination of rapid heating and pressureless sintering drastically reduces heat-up and dwell times, providing a fundamental advantage over slow conventional sintering.

1. Introduction

The Nd–Fe–B multiphase metallic system forms the foundation for permanent magnets, extensively used in various high-end applications such as computing, telecommunications, medical imaging, sensing, and energy conversion technologies.[1] Advanced magnets with the maximum energy products reaching

T. Tomše, A. Ivekovič, A. Kocjan, S. Šturm, K. Žužek
Department for Nanostructured Materials
Jožef Stefan Institute
Jamova cesta 39, SI-1000 Ljubljana, Slovenia
E-mail: tomaz.tomse@ijs.si

A. Kocjan, S. Šturm, K. Žužek
Jožef Stefan International Postgraduate School
Jamova cesta 39, SI-1000 Ljubljana, Slovenia

The ORCID identification number(s) for the author(s) of this article can be found under https://doi.org/10.1002/adem.202401404.

450 kJ m^{-3} are produced through conventional powder metallurgy routes. Sintering of micron-sized Nd–Fe–B-type powders prepared by standard procedures, i.e., strip casting, hydrogen decrepitation, and jet-milling,[2] is an energy-intensive process. It involves low heating rates—typically below 5 °C min^{-1}—toward sintering temperatures ranging from 1000 to 1100 °C, and the total heating time can reach 20 h.[3]

Contemporary sintering techniques such as ultrafast high-temperature sintering,[4] flash sintering,[5] and spark plasma sintering (SPS), also known as field-assisted sintering technology (FAST),[6] emphasize faster and more energy-efficient processes. Rapid heating, i.e., utilizing fast heating rates, shortens the time spent at high temperatures during the ramping phase, which reduces energy consumption. For instance, increasing the heating rate from 5 to 20 °C min^{-1} can decrease the energy required to heat a furnace to 1330 °C by ≈70%.[7] Importantly, sintering involves densification and grain growth, both driven by the minimization of the surface contribution to the energy of the system.[8] Higher heating rates may suppress the grain growth at intermediate temperatures to promote densification.[9] This inhibition of grain growth means that the material reaches high temperatures in a more sinterable state, which can reduce the dwell time at sintering temperatures required for densification, as observed for many ceramic materials, e.g., BaTiO$_3$,[7] yttria-stabilized zirconia,[9] ZnO,[10] and Al$_2$O$_3$.[11]

SPS is an electrical-current-activated, pressure-assisted technique characterized by rapid heating rates—several 100 °C min^{-1}—and short heating cycles. The versatile SPS enables fine-tuning of microstructure for a wide range of materials, such as nanostructured materials, ultrahigh-temperature ceramics, refractory metals, alloys, and composites. For powders that are more electrically conductive than the pressing die, the current flows through the sample as soon as the initial electrical paths are established.[6] However, an SPS approach to the manufacture of Nd–Fe–B magnets using standard powders has presented challenges. A typical microstructure of magnets primarily comprises the Nd$_2$Fe$_{14}$B hard-magnetic matrix phase accompanied by secondary phases rich in Nd, either metallic or oxides.[12] The magnetic performance of these materials is intricately linked to their chemical composition and microstructural features, namely, grain size and phase composition. Direct Joule heating

of the Nd–Fe–B material during SPS can facilitate the decomposition of the Nd$_2$Fe$_{14}$B matrix, owing to localized overheating at particle–particle contacts, leading to the formation of soft-magnetic α-Fe and drastic loss of hard-magnetic performance.[13]

SPS furnace can be adapted to a pressureless configuration, i.e., without the pressure being applied to the powder compact.[14] Additionally, by electrically and thermally insulating the compact from an electrically conductive crucible and by performing the sintering process in a vacuum environment, electrical power is dissipated in the crucible while the compact is indirectly heated through thermal radiation. This radiation-assisted sintering (RAS) approach allows for the crucible to be rapidly heated with heating rates as high as 500 °C min^{-1}.[15] However, the temperature of the sample, which is the heat sink for thermal radiation during heating, is not measured. RAS has demonstrated efficacy in rapidly sintering a variety of ceramic materials, including zirconia,[15–17] alumina,[11] potassium sodium niobate,[18] CrB$_2$,[19] SiC,[20] and Si$_3$N$_4$ foams,[21] as well as silica glass[22] and porous 3D printed titanium structures.[23]

Here, as a proof of concept, we employed the RAS approach to rapidly sinter a microcrystalline industrially used Nd–Fe–B powder. Notably, the Nd–Fe–B system undergoes eutectic transformation at ≈655 °C,[24] marking this work as the first report on RAS of a multiphase metallic material undergoing liquid-phase sintering. In the initial stage of liquid-phase sintering, the liquid phase facilitates particle rearrangement, followed by densification through solution–reprecipitation, while solid-state sintering can take place in the absence of the liquid phase.[25] In the intermediate stage, the liquid pressure dominates over the contribution of the solid–liquid interface energy, which initially increases with the formation of solid–liquid interfaces. Grain coarsening is not the essential mechanism driving densification in the initial and intermediate sintering stages. However, in the final sintering stage, when the liquid fills the smaller pores and when the pressure drops, grain coarsening accompanied by grain shape accommodation becomes the driving force for continued densification, as it reduces the solid–liquid interface energy.[26,27]

We investigated the impact of heating rate (10–200 °C min^{-1}) and dwell time (0–10 min) on the density, microstructure, and magnetic performance of RAS samples, assessing the potential benefits of rapid heating for microstructure refinement. Finite element modeling (FEM) was employed to calculate the sample's temperature during heating for moderate (25 °C min^{-1}) and fast (200 °C min^{-1}) heating rates. Our findings reveal that the final density is primarily influenced by the sample's final temperature and that high heating rates do not necessarily promote densification. Moreover, the RAS yielded grain size and microstructure closely comparable to those of conventionally sintered magnets prepared from the same powder. We attribute the substantial reduction in dwell times to the exceptional heat transfer efficiency via thermal radiation in RAS, which emerges as the most significant advantage over conventional sintering methods in terms of sintering cycle duration. Finally, we demonstrate that RAS overcomes the undesired current-related effects associated with SPS and effectively couples conventional pressureless sintering with rapid heating, enabling the manufacture of anisotropic Nd–Fe–B magnets without compromising the final magnetic performance.

2. Experimental Section

2.1. Nd–Fe–B Powder Compacts

The Nd–Fe–B-type powder with the composition Fe–30.0 Nd–3.0Co–1.0Dy–0.9B–0.6Pr–0.3O–0.2Ga–0.1Cu–0.1Al (wt%) was supplied by Magneti Ljubljana d.d. It was prepared using a standard powder-metallurgy method: the alloy underwent strip casting, and the resulting flakes were subsequently decrepitated with hydrogen to yield a coarse and friable powder. This coarse powder was then subjected to jet milling with nitrogen down to a mean particle size of 5.5 μm. To prepare the compacts, the milled powder without any lubricant was placed into a cylindrical silicon mold under a protective Ar atmosphere and vacuum sealed. The sealed powder was subjected to a pulsed magnetic field with a magnitude of 6 T to align the powder particles along the tetragonal c-axis of the Nd$_2$Fe$_{14}$B hard-magnetic phase. It was subsequently isostatically pressed under 800 MPa to achieve a relative density of ≈55%. The dimensions of the compacts were ≈17 mm (diameter) × 15 mm (height).

2.2. RAS

The powder compacts were sintered in a SPS furnace (SPS-632LxEx, Dr. SINTER, SPS Syntex Inc., Japan) under a dynamic vacuum in a custom-made cylindrical graphite crucible with an inner diameter of 38.4 mm and a height of 23.4 mm. The walls of the crucible were 4.2 mm thick. The compacts were placed in the center of the crucible on a 6 mm thick insulative graphite felt (Sigratherm GFA5, SGL Carbon) covered with protective boron nitride coating. Graphite felt exhibits approximately three orders of magnitude higher electrical resistivity and five orders of magnitude lower thermal conductivity compared to the crucible (refer to **Table 1**, Section 2.3). Due to the smaller diameter of the compact relative to the inner diameter of the crucible (≈17 and 38.4 mm, respectively), the compact is electrically insulated from the crucible. Under such noncontact conditions, most of the electrical current flows through the crucible that consequently gets hot, hence it represents a heat source, i.e., the radiator, as described elsewhere.[16] A schematic illustration of the setup is shown in **Figure 1**. The Inconel electrodes were water-cooled. For all RAS experiments, the heating of the crucible was initiated at room temperature (RT). The temperature was measured on the crucible wall with a pyrometer. Below the visible range of the pyrometer at 570 °C, the current increase was preset. Above the visible range, the heating was temperature-controlled. The temperature, the electrical current, and voltage during heating were recorded, and the current data were used as an input for FEM modeling (Section 2.3). The energy consumption was calculated based on the current and voltage profiles. For this purpose, to minimize the radiative heat loss from the external surfaces of the crucible, the latter was wrapped in the insulative graphite felt, leaving only a 5 mm opening at the specimen level for temperature control.

The effect of RAS parameters on the sample's temperature, final density, microstructure formation, and magnetic performance was studied. Notable controlled parameters were the heating rate (10–200 °C min^{-1}), the maximum temperature of the crucible, i.e., sintering temperature—T_{SINT} (1100–1200 °C),

Table 1. Physical properties of materials used in the FE calculations (with temperature—T in Kelvin).

|	Inconel[29]	Graphite[29]	Graphite felt[a]	Nd–Fe–B[41]
Heat capacity—C_p [J kg^{-1} K^{-1}]	344 $+2.5 \times 10^{-1}$ T	34.27 $+2.72$ T -9.60×10^{-4} T^2	200	502.42
Thermal conductivity—k [Wm^{-1} K^{-1}]	10.09 $+1.57 \times 10^{-2}$ T	123 -6.99×10^{-2} T $+1.55 \times 10^{-5}$ T^2	0.0061 $+8 \times 10^{-5}$ T -1×10^{-7} T^2 $+8 \times 10^{-11}$ T^3	8.96
Electrical resistivity—ρ_e [Ωm]	9.82×10^{-7} $+1.6 \times 10^{-10}$ T	2.14×10^{-5} -1.34×10^{-8} T $+4.42 \times 10^{-12}$ T^2	0.01	1.5×10^{-6}
Density—ρ [kg m^{-3}]	8430	1904 -0.01414 T	120	7500
Emissivity—ε	0.67	0.8	0.3	0.6

[a] Data provided by the manufacturer.
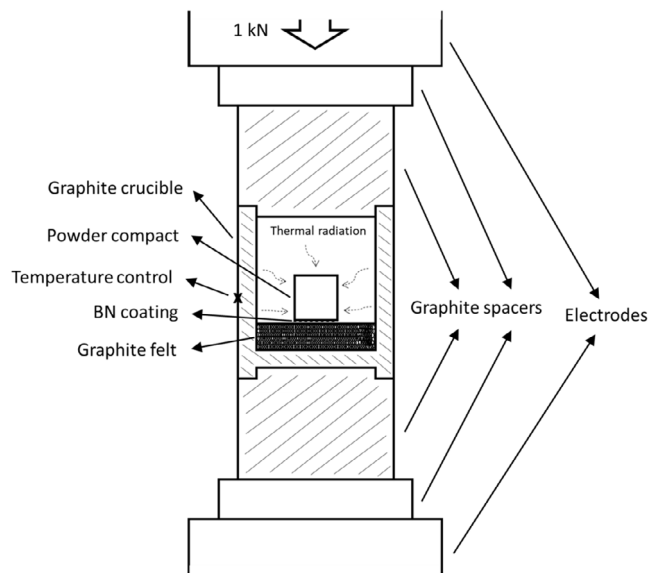
Figure 1. Schematic illustration of the RAS setup (cross section).

and dwell time at $T_{\mathrm{SINT}} - t_{\mathrm{DWELL}}$ (0–10 min). After t_{DWELL}, the power was turned off and the sample-containing crucible was left to cool naturally.

The Nd–Fe–B powder material contained interstitial and bonded hydrogen which is progressively thermally desorbed during heating to ≈600 °C.[28] Two different heating strategies were considered: i) *Two-step heating*: In the first step, the current was programmed to steadily increase from RT to 570 °C (the visible range of the pyrometer), giving the average heating rate at ≈40 °C min^{-1}. This precaution was taken to prevent rapid pressure increase in the SPS chamber due to hydrogen desorption. The temperature of the crucible then stabilized at 650 °C within 2 min. In the second heating step from 650 °C to T_{SINT}, the heating rate was varied. The pressure during heating varied from initial ≈3×10^{-3} to ≈1×10^2 Pa; and ii) *Rapid heating from RT*:

Below 570 °C (the visible range of the pyrometer), the current was preset in a way that the average heating rate was ≈150 °C min^{-1} from RT to 1100 °C of T_{SINT}. The dwell time at T_{SINT} was 2 min. In this case, the pressure during heating peaked at ≈7×10^2 Pa.

2.3. FEM

Finite element simulation of the RAS process was conducted utilizing the COMSOL Multiphysics software package with a fully coupled Joule heating module, combining electrical currents with thermal conduction through solid, and the surface-to-surface radiation module. The temperature distribution within the system was calculated by solving the partial differential equations described in the literature.[29] To reduce the unnecessary complexity of modeling, several assumptions regarding the system and the initial boundary conditions were applied. As the sintering was conducted in a vacuum, the heat losses by conduction or convection through gas were neglected. The 2D axisymmetric model was applied using the experimentally measured electrical current as the input data. The geometry of the RAS setup showing boundary conditions used in FEM simulations is shown in **Figure 2**.

Bulk material properties used for the calculation are listed in Table 1. They were obtained from the literature and material suppliers. Limiting conditions have been imposed on the outer vertical and horizontal boundaries: a radiative heat flux was assumed on all the outer vertical walls of electrodes, spacers, crucible, and punches, with surface emissivity values depending on the material (see Table 1) and the ambient temperature set at 300 K. A convective heat flux (heat transfer coefficient $h_c = 100$ W m^{-2} K^{-1}, constant water temperature of 300 K) was assumed for the electrode surfaces in contact with the cooling system. Electrical and thermal contact resistances at the electrode–spacer and spacer–spacer interfaces were used to calibrate the simulation to obtain a good fit between the simulated and experimentally measured temperature values at the outer diameter of the crucible (see Figure 2).

**ADVANCED
SCIENCE NEWS**

www.advancedsciencenews.com

**ADVANCED
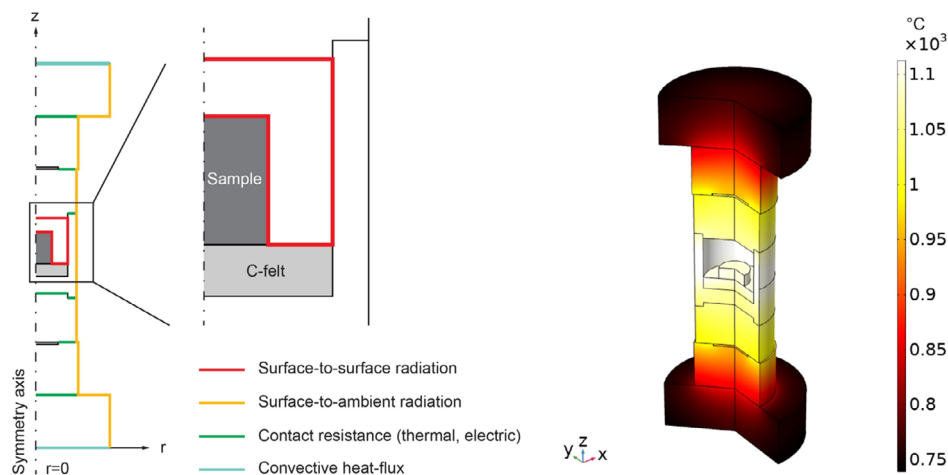ENGINEERING
MATERIALS**

www.aem-journal.com

Figure 2. Left: Schematic representation of the 2D axisymmetric geometry of the RAS furnace column with indicated boundary conditions used in FEM simulations. Right: Calculated temperature distribution in the experimental setup during dwell time at 1100 °C.

2.4. Conventional Vacuum Sintering and Postsinter Annealing

Slow vacuum sintering and postsinter annealing (PSA) of RAS and conventionally sintered samples were performed in a tube furnace (Carbolite) in a 5×10^{-5} mbar vacuum. Sintering to full density was performed by heating a powder compact at the $3\,°C\,min^{-1}$ heating rate from RT to 1070 °C. The dwell time was 120 min. The cooling rate, which was not controlled, following heating, was $\approx 9\,°C\,min^{-1}$ in the 1070 to 600 °C range. The sintering parameters were optimized for the Nd–Fe–B powder used in this study. A second sintered sample was prepared by applying the $5\,°C\,min^{-1}$ heating rate to 1100 °C and 5 min of dwell time.

PSA of selected samples was performed at 520 °C for 2 h. The heating rate to the annealing temperature was $3\,°C\,min^{-1}$. The temperature was optimized for the material used and agrees with the usual PSA conditions for sintered Nd–Fe–B magnets.[30] An intermediate postsintering heat treatment, e.g., at 820 °C as reported in ref. [30], did not prove beneficial for the final coercivity.

2.5. Characterization

The samples' absolute densities were determined based on Archimedes' principle with a density meter (Densitec) by immersing them in silicone oil. Microstructural investigation of the Nd–Fe–B powder and bulk samples was performed with a field-emission-gun scanning electron microscope (SEM) JEOL JSM-7600F equipped with an energy-dispersive X-ray spectroscopy detector (INCA system, Oxford Instruments, UK). Backscattered-electron (BSE) imaging in compositional contrast mode was used to observe the major crystalline phases. For the investigation, the samples were embedded in a resin (EpoFix Kit Resin and hardener from Struers) and metallographically polished with isopropanol-based suspensions of 3 and 0.25 μm diamond paste. Polished surfaces of selected samples were chemically etched with an HCl-saturated Cyphos IL 101 ionic liquid to expose the grain boundaries. The apparent average grain size was determined from SEM images by measuring the diameter of 200 grains. The as-obtained value represents the average projected grain diameter in the 2D image. Assuming the grains were equiaxed, the actual grain size was estimated by multiplying the apparent, i.e., measured, grain size by the shape factor 1.5. Magnetic measurements were performed by applying a closed-loop hysteresisgraph (Permagraph, Magnet-Physik) at RT (as-sintered samples) and 50 °C (PSA samples). The measurement uncertainty of the values obtained with a hysteresisgraph was less than 2%.

3. Results

3.1. Two-Step Heating

3.1.1. RAS Parameters and Density

The dependence of the bulk density on T_{SINT} for RAS samples prepared with $100\,°C\,min^{-1}$ heating rate without dwell time is shown in **Figure 3**a. The density increases with T_{SINT} and reaches $7.49\,g\,cm^{-3}$, or $\approx$98% of full density, at 1200 °C. To minimize the risk of the decomposition of the matrix phase and formation of soft-magnetic α-Fe phase when heating above the peritectic temperature of the Nd–Fe–B ternary system at $\approx$1180 °C,[24] T_{SINT} was set to 1100 °C for further parametric study. Figure 3b shows the dependence of the bulk density on t_{DWELL} at 1100 °C (T_{SINT}) for heating rates ranging from 10 to 200 °C. For the very slow $10\,°C\,min^{-1}$ heating rate, full density ($7.63\,g\,cm^{-3}$) is reached at $t_{DWELL} = 0$ min and does not change when t_{DWELL} is increased. The density at $t_{DWELL} = 0$ min gradually drops to 93, 85, 83, and 81 rel.% when the heating rate is increased to 25, 50, 100, and 200 °C min^{-1}, respectively. For the 25–200 °C min^{-1} heating rate, the density increases with dwell time and the compacts densify within 5 min of t_{DWELL}. For comparison, the density of a conventionally sintered sample, prepared with a heating rate of 5 °C min^{-1} to 1100 °C and 5 min of t_{DWELL} reached only 94 rel.% of the density of RAS samples (star symbol in Figure 3b).
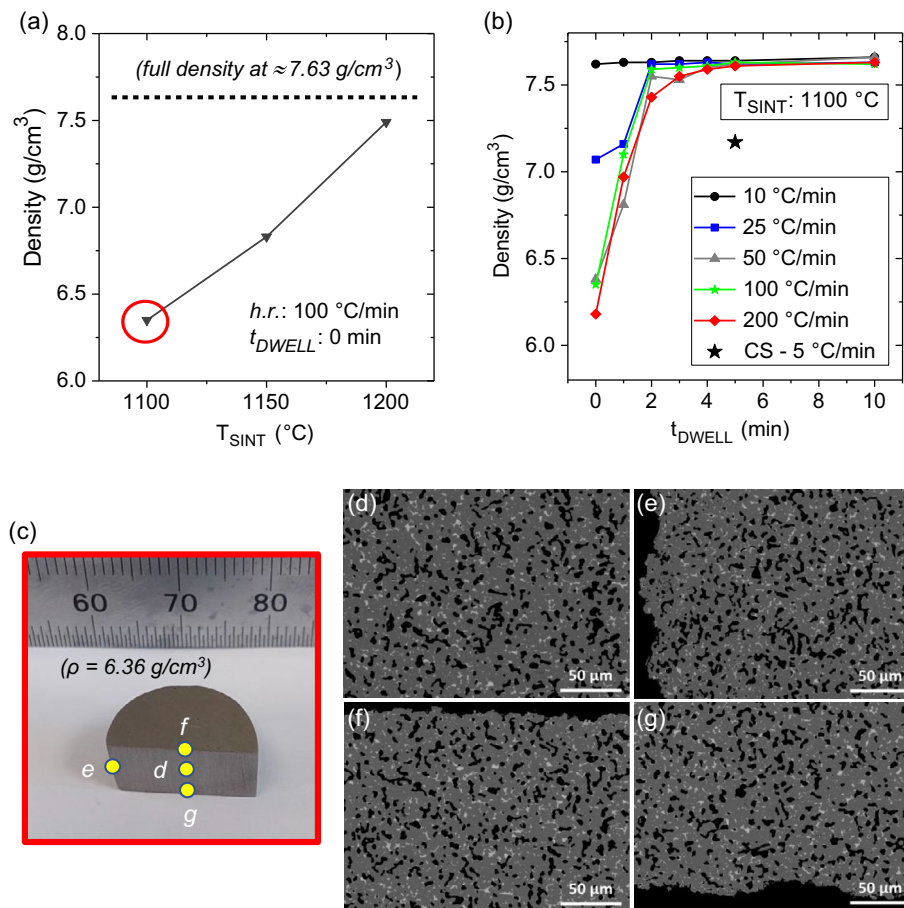
Figure 3. Effect of RAS parameters on density. a) Dependence of the bulk density on the sintering temperature (T_{SINT}) for 100 °C min^{-1} of heating rate and no dwell time at T_{SINT}. b) Dependence of the bulk density on the dwell time—t_{DWELL}; the heating rate was varied between 10 and 200 °C min^{-1}. For comparison, the star symbol marks the density of a conventionally sintered sample with 5 min of t_{DWELL} at 1100 °C. c) Photo of the low-density RAS sample, prepared with 100 °C min^{-1} of heating rate with no dwell time at 1100 °C. The cylindrical sample was cut in half along its axis. Locations of the BSE-SEM analysis are marked on its cross section: d) center, e) side edge, f) upper edge, and g) bottom edge.

Microstructural homogeneity of a low-density RAS sample ($\rho = 6.36$ g cm^{-3} or 84 rel.%), prepared with 100 °C min^{-1} of heating rate and no dwell time at 1100 °C, was investigated through SEM imaging to asses if densification during heating is even throughout the powder compact's volume. The sample's cross section with marked areas of the SEM analysis is shown in Figure 3c. The sample was found to be highly porous, consistent with its low density. Its center region (Figure 3d), the edges corresponding to the circular plane surfaces (Figure 3f,g, respectively), and the side edge (Figure 3e) display comparable levels of porosity.

3.1.2. FEM Study

Experimental electrical current and temperature profiles for a moderate 25 °C min^{-1} heating rate (sample R25) and a fast 200 °C min^{-1} heating rate (sample R200) are shown in **Figure 4**a. Note that the temperature was not measured below 570 °C. In both cases, T_{SINT} was 1100 °C and t_{DWELL} was 5 min. Up to 570 °C, the current steadily increases (dotted blue

and red curves for samples R25 and R200, respectively). In this first heating step, the current was preset and is therefore identical for the two samples. In the second heating step, the current increases until the crucible temperature, shown by the full blue and red curves for samples R25 and R200, respectively, reaches T_{SINT}. Even for the very fast heating rate of 200 °C min^{-1}, the RAS approach offers excellent control of the crucible temperature, which did not overshoot at the beginning of the dwell stage and remained constant throughout the isothermal step. The dwell stage is followed by fast cooling. Figure 4b compares the measured temperature of the crucible (full curves) with the modeled crucible temperature—T_{CM} (dashed curves) and the modeled sample temperature—T_{SM} (dotted curves). The modeled crucible temperature matches the temperature as measured in the 570–1100 °C range, confirming that the FEM model can reliably predict the temperature based on the current, recorded during RAS. Importantly, the model provides information on the temperature below 570 °C, which is not obtained by the measurement. The FEM study also revealed that T_{SM} lagged behind T_{CM} throughout the heating. Moreover, the

ADVANCED
SCIENCE NEWS
www.advancedsciencenews.com

ADVANCED
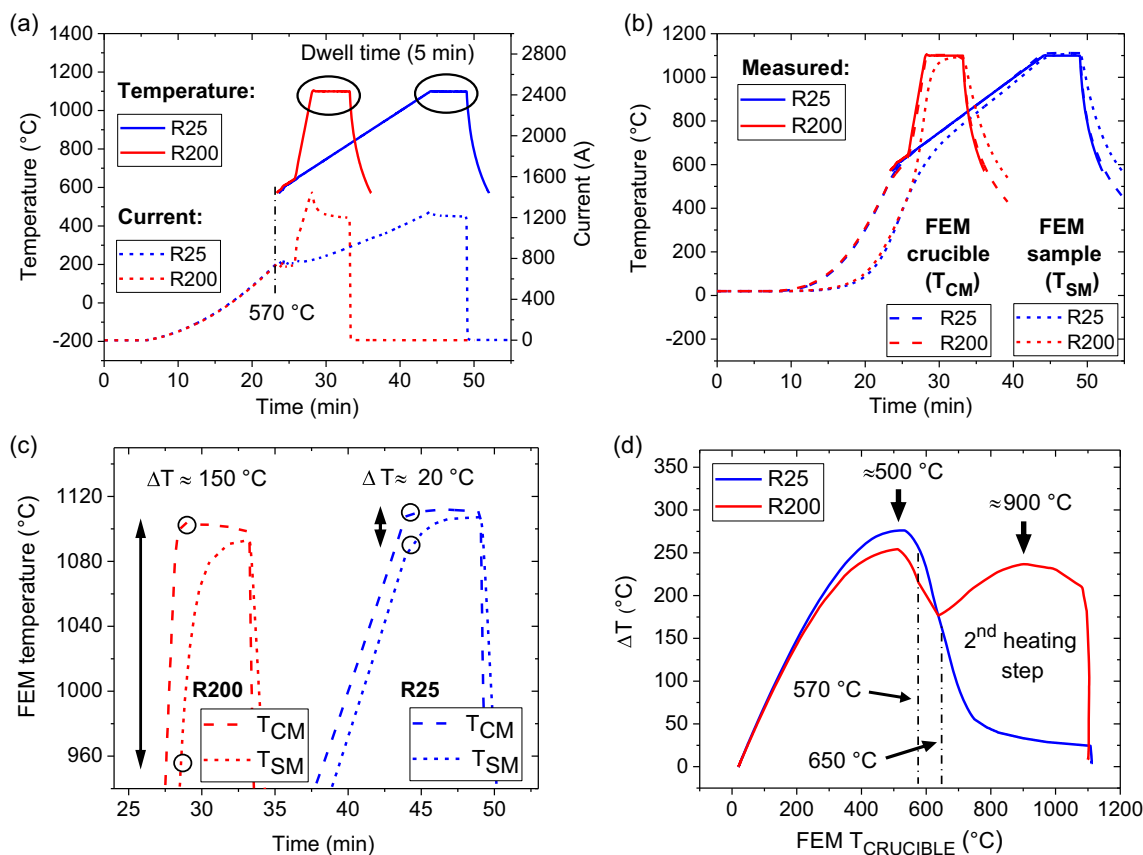ENGINEERING
MATERIALS
www.aem-journal.com

Figure 4. Experimental data and modeled temperature for samples R25 and R200. a) Electric current profiles and the temperature of the crucible measured with the pyrometer. The temperature was not recorded below 570 °C. b) The measured temperature of the crucible and FEM crucible temperature (T_{CM}) and sample temperature (T_{SM}) calculated based on the electric current profile and temperature of the crucible, respectively. c) The modeled temperature of the crucible (T_{CM}) and of the sample (T_{SM}) close to T_{SINT} showing the temperature difference between T_{CM} and T_{SM} (ΔT) at the dwell start at 1100 °C. d) Temperature difference (ΔT) in relation to the modeled temperature of the crucible (T_{CM}) with indicated visible range of the pyrometer at 570 °C and beginning of the second heating step at 650 °C.

difference between T_{CM} and T_{SM} (temperature difference—ΔT) is more pronounced for the higher heating rate. As shown in Figure 4c, when T_{CM} reaches T_{SINT}, ΔT is ≈150 and ≈20 °C, respectively, for samples R200 (red curves) and R25 (blue curves). During the dwell stage, the increase in sample temperature levels off ($\Delta T < 10$ °C) after ≈1 and 5 min for samples R25 and R200, respectively. Figure 4d shows ΔT for samples R25 (blue curve) and R200 (red curve) with respect to crucible temperature (T_{CM}). From the beginning of heating, ΔT is steadily increasing and peaks at ≈500 °C. For sample R25, ΔT decreases with further temperature increase until the heating is terminated. On the other hand, for sample R200, ΔT increases again at 650 °C, corresponding to the beginning of the second heating step, and a second maximum can be observed in the red curve at ≈900 °C.

Figure 5 compares T_{SM} for sample R200 during the dwell stage and dependence of bulk density on t_{DWELL} for samples prepared with 200 °C min^{-1} heating rate (shown also in Figure 3b, red curve). The dwell start (0 min) is the time when the measured temperature of the crucible reaches 1100 °C (T_{SINT}). The density and T_{SM} both rapidly increase in the first two minutes of t_{DWELL}.
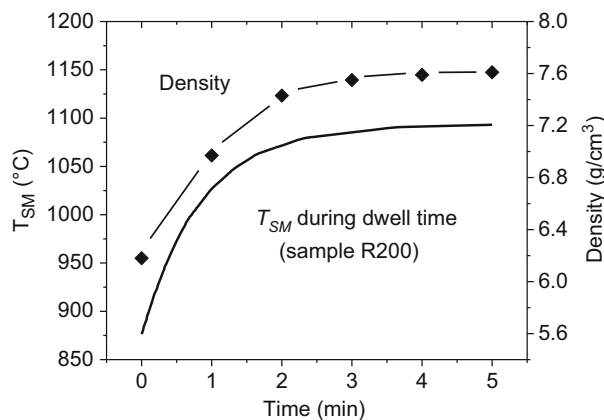

Figure 5. FEM temperature (T_{SM}) of sample R200 during dwell time at 1100 °C and dependence of bulk density on dwell time for samples prepared with 200 °C min^{-1} of heating rate.

At this point, the density is 7.43 g cm^{-3} or 97.6% of maximum density (7.61 g cm^{-3}), and T_{SM} is 1072 °C or 97.9% of the maximum T_{SM} reached after 5 min (1095 °C). Between 2 and 5 min of

2401404 (6 of 12)

t_{DWELL}, the density and T_{SM} continue to increase at a lower rate and stabilize toward the end of the dwell stage.

3.1.3. Effect of Heating Rate on Magnetic Performance and Final Microstructure

The room-temperature magnetic properties (remanence—B_r, maximum energy product—$(BH)_{max}$, and intrinsic coercivity—H_{ci}), squareness factor—SF, and densities of selected RAS samples prepared with different heating rates and 1100 °C of T_{SINT} are collected in **Table 2**. All RAS samples were prepared with 5 min of t_{DWELL} at T_{SINT}, except for sample R10 which was prepared without dwell time. Process parameters and properties of a conventionally sintered sample are added for comparison.

Room-temperature demagnetization curves, measured for the fully dense as-sintered RAS samples prepared at different heating rates, i.e., R10, R25, R50, R100, R200, and a conventionally sintered sample CS3, are shown in **Figure 6**a. The samples' B_r values (1.32–1.35 T) and $(BH)_{max}$ values (336–352 kJ m^{-3}), collected in Table 2, are similar. The SF of the demagnetization curves, defined as H_k/H_{ci} where H_k is the knee point field at $0.9B_r$ and H_{ci} is intrinsic coercivity, ranges between 0.89 and 0.95 for RAS samples. In comparison, the SF value is 0.96 for sample CS3. Such values are typical for anisotropic sintered Nd–Fe–B magnets.[31]

The H_{ci} values of RAS samples range between 565 and 670 kA m^{-1}, while the intrinsic coercivity of the conventionally sintered sample CS3 is higher (870 kA m^{-1}). Figure 6b shows demagnetization curves, measured at 50 °C, for samples R25, R200, and CS3, before (dashed curves) and after (full curves) PSA. The as-sintered H_{ci} improved with PSA to comparable values. For both RAS samples, the increase was substantial: ≈110% for sample R25 (from 485 to 1030 kA m^{-1}, blue curves) and ≈80% for sample R200 (from 551 to 1005 kA m^{-1}, red curves). In comparison, for the conventionally sintered sample CS3, the H_{ci} was increased by ≈45% (from 710 to 1020 kA m^{-1}, green curves) upon PSA.

BSE-SEM images of PSA samples R25, R200, and CS3 are shown in **Figure 7**a–c, respectively. As is typical for fully dense, sintered, Nd–Fe–B-type permanent magnets,[12] the microstructures, which appear identical, consist of $Nd_2Fe_{14}B$ phase (gray matrix) and secondary phases rich in Nd displaying a brighter contrast in the backscattered imaging mode. No porosity was observed, consistent with the high bulk density. The grain structure, exposed by acid leaching of the polished cross sections, is shown in Figure 7d–f for samples R25, R200, and CS3, respectively. The average grain size was estimated at 11.3, 11.2, and 10.7 μm for samples R25, R200, and CS3, respectively. Compared to the average particle size of the initial powder (5.5 μm), the grains in sintered samples

Table 2. Room-Temperature magnetic properties and densities of selected samples prepared via the RAS approach.

Sample	T_{SINT} [°C]	Heating rate [°C min^{-1}]	t_{DWELL} [min]	B_r [T]	$(BH)_{max}$ [kJ m^{-3}]	H_{ci} [kA m^{-1}]	SF $= H_k/H_{ci}$	ρ [g cm^{-3}]
R10	1100	10	0	1.32	336	565	0.94	7.62
R25	1100	25	5	1.34	352	630	0.90	7.63
R50	1100	50	5	1.34	348	590	0.94	7.62
R100	1100	100	5	1.34	342	615	0.89	7.63
R200	1100	200	5	1.34	346	670	0.95	7.61
CS3[a]	1070	3	120	1.34	347	870	0.96	7.63

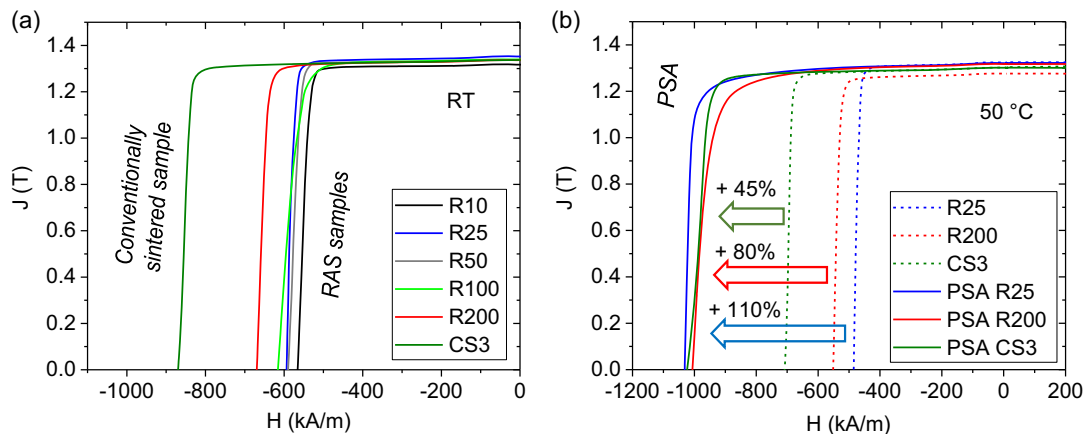[a]A fully dense conventionally sintered sample is added for comparison.

Figure 6. Magnetic properties of fully dense samples. a) Room-temperature demagnetization curves of as-sintered RAS samples prepared with different heating rates (R10–R200) and of a conventionally sintered sample CS3. b) Demagnetization curves of as-sintered and PSA RAS samples R25 and R200 and of a conventionally sintered sample CS3, measured at 50 °C.
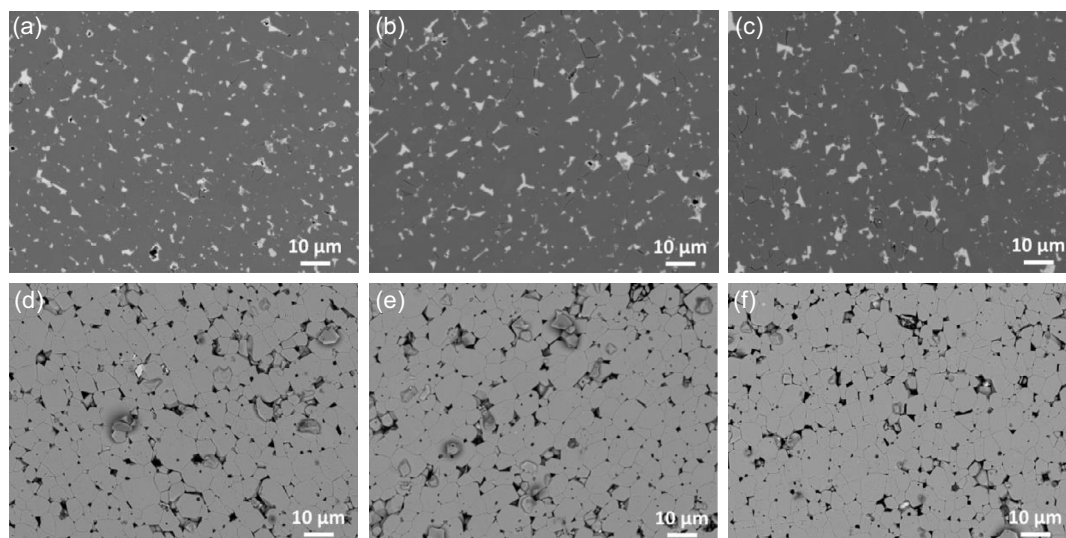
**ADVANCED
SCIENCE NEWS**

www.advancedsciencenews.com

**ADVANCED
ENGINEERING
MATERIALS**

www.aem-journal.com

Figure 7. BSE-SEM images of polished and etched cross sections of PSA samples. Polished cross sections: a) R25, b) R200, and c) CS3. Etched cross sections: d) R25, e) R200, and f) CS3.

are larger by a factor of ≈ 2, as expected for sintered Nd–Fe–B magnets.[32]

3.1.4. Energy Consumption

The energy consumption for typical RAS cycles used in this study is shown in **Table 3**. For the low heating rate (10 °C min^{-1}), the energy input is 9.73 MJ when the graphite crucible is not thermally insulated with the graphite felt. It decreases to 6.54 MJ for the moderate (25 °C min^{-1}) heating rate, despite the introduction of 5 min of dwell time. The energy consumption is further reduced to 3.53 MJ when the heating rate is increased to 200 °C min^{-1}. Insulating the crucible to minimize the radiative heat loss reduced the energy consumption by 27%–35%.

3.2. Rapid Heating from RT

A RAS run based on rapid heating from RT is demonstrated in **Figure 8**. Figure 8a shows the recorded electric current profile (blue curve) and the temperature of the crucible (dashed red curve). The electric current (blue curve) continuously increases from the start of heating to the sintering temperature (T_{SINT}) at 1100 °C, with a minor setback at 570 °C when the pyrometer starts recording data and the heating process becomes temperature-controlled. The average heating rate in this case

Table 3. Energy consumption for different heating cycles.

Heating rate [°C min^{-1}]	Dwell time [min]	Energy consumption— without insulation [MJ]	Energy consumption—with insulation [MJ]
10 (slow)	0	9.73	6.34
25 (moderate)	5	6.54	4.23
200 (fast)	5	3.53	2.56

was ≈ 150 °C min^{-1}. The sample's room-temperature demagnetization curve is shown in Figure 8b. As was the case for samples prepared with a two-step heating procedure (Table 2), it is characterized by a high degree of squareness, with 1.35 T of remanence and 610 kA m^{-1} of intrinsic coercivity. Although the total heating time, i.e., ramping and dwell stage, was only 9.15 min, the initial near-monocrystalline powder, shown in Figure 8c, was successfully densified, and the microstructure of the final sample shown in Figure 8d is homogeneous.

4. Discussion

4.1. Magnetic Performance

The coercivity of Nd–Fe–B magnets is governed by the interaction of local inherent magnetic characteristics and nanoscale magnetization processes.[33] Lower H_{ci} values of as-sintered RAS samples compared to sample CS3 (565–670 and 870 kA m^{-1}, respectively, Table 2) are explained by differences in the cooling rates between RAS and conventional sintering. Fast cooling after the sintering cycle can hinder the development of coercivity, as it results in distorted interfaces between the thin grain-boundary film and matrix grains due to the rapid solidification of the liquid.[30,34] In RAS, the heat dissipates from the crucible fast via radiation and conduction through spacers and water-cooled electrodes after the heating is terminated. Hence, according to FEM calculations (Figure 4b), T_{SM} rapidly drops through radiation heat loss, with an average cooling rate higher than 100 °C min^{-1} in the 1100–600 °C range. For conventional sintering, the cooling rate in the same temperature range is slower by an order of magnitude (Section 2.4). The cooling rate during RAS was not controlled and is presumed to vary between different sintering cycles due to the varying amounts of heat accumulated in the setup, which could affect the as-sintered coercivities. Importantly, H_{ci} values of RAS samples improved
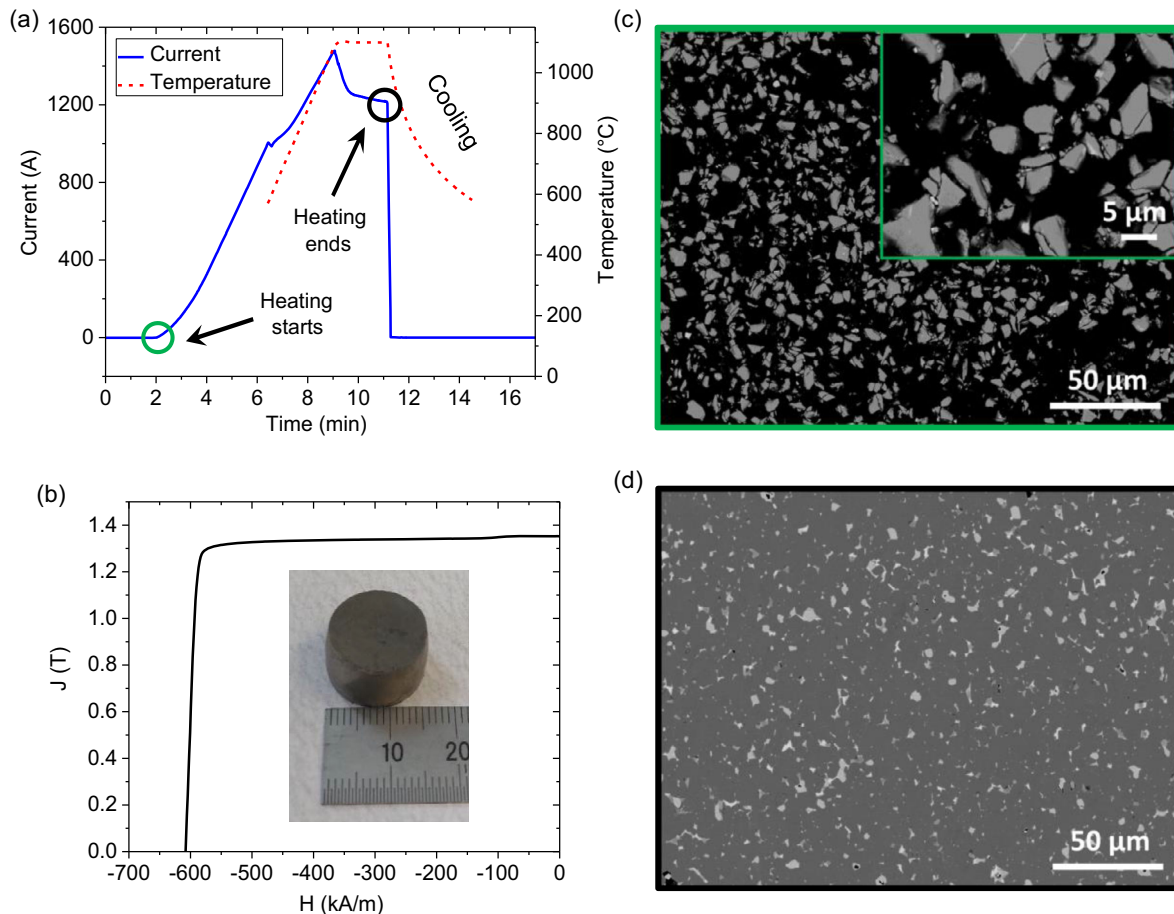
Figure 8. Microcrystalline Nd–Fe–B-type powder rapidly sintered to full density within 9.15 min. a) RAS process data: electrical current and as-measured temperature profiles with marked start and end of heating. The temperature was not recorded below 570 °C. b) Room-temperature demagnetization curve and a photo of the as-sintered RAS sample. c) BSE-SEM image of the cross section of the initial powder embedded in a resin with a higher magnification image in the inset. d) BSE-SEM image taken on the sintered sample's cross section.

significantly after PSA (Figure 6b) and reached the coercivity of sample CS3 ($\approx$1000 kA m^{-1} at 50 °C). For Nd–Fe-B magnets, the increase in H_{ci} with PSA has been ascribed to: i) the formation of a few nanometer-thick and continuous Nd-rich layer at the grain boundaries, ensuring magnetic insulation of grains; ii) the elimination of structural distortions, leading to smooth interfaces between thin film and matrix grains; and iii) phase transformations of secondary phases.[30,35] For the samples prepared via RAS, achieving an optimal grain size of $\approx$5 µm or less, which is ideal for high-performance magnets, would be the future key goal. Currently, the grain size stands at about $\approx$11 µm, highlighting the importance of refining the mean powder particle size to around 3 µm for enhanced coercivity.[32,36]

The samples' B_r and $(BH)_{max}$ values, comparable to the values of the conventionally sintered sample CS3, classify them as N45 magnet grade, in agreement with the material's chemical composition, namely, the addition of 1 wt% of Dy (Section 2.1) which decreases the saturation magnetization of the Nd$_2$Fe$_{14}$B hard-magnetic phase.[37] The remanence depends on the density, phase composition, and crystallographic texture achieved through magnetic alignment of the powder particle before

pressing (Section 2.1). Correspondingly, the high B_r values reflect the samples' full density and suggest a comparable crystallographic texture and phase distribution. Moreover, the high degree of squareness confirms the absence of microstructural inhomogeneities. The results of magnetic characterization highlight the feasibility of the RAS approach for rapid sintering of anisotropic Nd–Fe-B-type magnets.

4.2. Sample Temperature during RAS

The bulk density of RAS samples increases with T_{SINT} for the 100 °C min^{-1} heating rate and no dwell time at T_{SINT} (Figure 3a), confirming that the density primarily depends on the temperature, as was expected. The gradual decrease in density of RAS samples prepared without dwell time at 1100 °C when the heating rate was increased from 10 °C min^{-1} (fully dense) to 200 °C min^{-1} (81 rel.% density), Figure 3b, is interpreted concerning the sample's temperature. FEM analysis revealed that T_{SM} was only $\approx$950 °C at the dwell start (Figure 4c) for the fastest heating rate (sample R200). Importantly, the calculated temperature of sample R200 during t_{DWELL} and dependence of bulk

**ADVANCED
SCIENCE NEWS**

www.advancedsciencenews.com

**ADVANCED
ENGINEERING
MATERIALS**

www.aem-journal.com

density on t_{DWELL} for samples prepared with 200 °C min^{-1} heating rate show the same trend of increase (Figure 5). It is concluded that the sample's maximum temperature, which depends on the heating rate and dwell time at T_{SINT}, determines the final density. The short dwell time of up to 5 min allows for the temperature of the sample to level off for high heating rates; however, isothermal heating, in terms of the sample's temperature, is not necessary to ensure full densify at optimized T_{SINT}.

The uniform porosity of a low-density sample (84 rel.% density), prepared with 100 °C min^{-1} of heating rate and no dwell time at T_{SINT}, throughout its volume (Figure 3d–g), reveals that the temperature field in the sample during heating was homogeneous. Any significant temperature gradients in the sample would result in local variation of density, considering the established dependence of the density on the sample's temperature, which was not the case. This indicates fast heat dissipation in the compact. A rapid heat transfer within the sample was also reported for 3% yttria partially stabilized zirconia (3Y-TZP) with a low thermal conductivity that was rapidly densified via RAS without cracks, shape distortions, or density gradients.[15] However, in the case of 3Y-TZP powder, the average particle size was 80 nm, which is almost two orders of magnitude smaller than the Nd–Fe–B powder used in the present study. Smaller pores in 3Y-TZP material could favor internal scattering of the thermal radiation, and the very small particles could even be transparent for certain wavelengths, meaning that the radiation can penetrate deeper into the powder compact, which favors uniform densification.

4.3. RAS and Microstructure Formation

As shown in Figure 4d, the temperature difference between the sample and crucible (ΔT) is larger than 150 at 650 °C of T_{CM}, i.e., at the beginning of the second heating step. This means that the temperature of the sample in the first heating step is less than 500 °C and significantly below the eutectic temperature (T_{EUT}) of the Nd–Fe–B ternary system at ≈655 °C.[24] Correspondingly, the liquid phase is absent in the first heating step and the heating rate below T_{EUT} is expected to have a negligible effect on the final microstructure.

Particle rearrangement following the formation of the liquid phase is the initial densification mechanism in liquid-phase sintering. In the Nd–Fe–B system, it could disrupt the crystallographic texture of the magnetically anisotropic powder compacts, decreasing the remanence of final magnets. Therefore, the relevance of the heating rate for the particle rearrangement can be assessed by comparing the remanence of samples prepared under different conditions. Because the RAS samples and a conventionally sintered sample have similar B_r values (≈1.34 T, Table 2), the contribution of the rearrangement to total densification must be similar for the two sintering techniques and is not significantly affected by the heating rate.

SEM analysis of RAS samples and a conventionally sintered sample CS3 disclosed comparable microstructures (Figure 7 and 8d). Demonstrably, the RAS offers an important advantage over hot-pressing SPS where the nonequilibrium conditions can lead to undesired phase transformations, namely, the formation of soft-magnetic α-Fe precipitates.[13] Due to a highly negative

reduction potential of the neodymium (−2.32 V),[38] acid etching of the samples' polished surfaces selectively removed the secondary Nd-rich phases to reveal a contour of continuous solidified liquid network and faceted grains, as seen in Figure 7d–f. Such a microstructure is typical of solution-reprecipitation stage densification.[25] Moreover, the grain sizes of RAS and CS samples are comparable (Section 3.2.3) and independent of the heating rate. These findings indicate that fast heating rates (up to 200 °C min^{-1} in this study) did not significantly alter the sintering mechanisms to favor densification during the initial and intermediate sintering stages, where particle rearrangement and liquid pressure are the primary driving forces, over grain coarsening.

4.4. Heat Transfer in RAS and Energy Efficiency

As rapid heating in RAS does not lead to microstructure refinement in the Nd–Fe–B samples, the reduction in dwell time compared to conventional sintering cannot be attributed to enhanced densification through the suppression of grain growth during ramping, as observed in ceramics where the driving force for densification is amplified by the smaller particle size.[7,9–11] Additionally, full density is achieved without any dwell time even with a relatively slow heating rate of 10 °C min^{-1}, suggesting that high heating rates do not necessarily promote densification.

The reduction in dwell time can be understood by considering the specifics of the experimental setup and the heat transfer mechanism in RAS. In this process, electric power is used to heat the graphite crucible, acting as the radiator, in a controlled manner. At elevated temperatures, thermal radiation is the most efficient heat transfer mechanism. The radiative flux density (W m^{-2}) diminishes with distance from the radiator.[39] Here, the distance between the compact and the crucible walls is only 10.5 mm before the shrinkage, which is beneficial for reaching thermal equilibrium in a short time, resulting in very efficient heating.

Heidary et al.[7] conducted a comparative analysis of the energy consumption required to sinter BaTiO$_3$ powder across various sintering methodologies at a laboratory scale. Their findings revealed that the energy demand amounted to 2.8 MJ g^{-1} for slow conventional sintering, 1.05 MJ g^{-1} for FAST, and 0.13 MJ g^{-1} for rapid sintering in a laboratory furnace, marking more than a tenfold reduction in energy consumption compared to slow heating methods.[7] In our investigation, considering that the Nd–Fe–B samples prepared with RAS weighted ≈15 g, the minimum energy consumption for a heating rate of 200 °C min^{-1} (as detailed in Table 3) amounts to 0.17 MJ g^{-1}, aligning closely with the energy efficiency achieved through rapid sintering as reported in.[7] This straightforward comparison underscores the promising potential of the RAS approach for rapid and energy-efficient sintering cycles.

The values presented in Table 3 are specific to the experimental setup used in this study and the energy consumption per gram would be considerably lower for larger samples. Moreover, the RAS experiments were performed in a laboratory-scale SPS furnace intended for hot-pressing applications, which is not optimized to minimize heat dissipation via radiation and conduction through the graphite spacers. For instance, the

Inconel electrodes are water-cooled to prevent setup overheating, leading to significant energy dissipation. This suggests that further reductions in energy input could be achievable using more specialized furnaces designed specifically to reduce such losses.

Although the present study demonstrated the production of one piece per cycle, scalable manufacturing processes for SPS and related methods have already been proven, allowing for the throughput of several pieces per minute.[40] These advancements indicate a promising pathway for adapting the proposed RAS strategy to larger-scale production. Future research should focus on furnace designs that would enable simultaneous sintering of multiple pieces while maintaining the reduced energy consumption observed at the laboratory scale. This optimization would be crucial for developing competitive batch production processes that could rival conventional sintering methods in the industry. In summary, further work is needed to validate the energy efficiency of the RAS approach when scaled up to the batch sizes of hundreds of kilograms commonly used in industrial processes.

5. Conclusions

This study highlights the prospect of the RAS strategy for rapid processing of microcrystalline Nd–Fe–B-type multiphase metallic powders. RAS offers precise control over the radiator's temperature, while FEM enables calculation of the sample's temperature during heating. Fully dense Nd–Fe–B magnets are prepared across several heating rates (ranging from 10 to $200\,°C\,min^{-1}$) with significantly reduced dwell times (up to 5 min) at the sintering temperature of $1100\,°C$, as compared to the time-intensive, hour-long conventional vacuum sintering. The magnetic properties of RAS samples—remanence ($1.32–1.35\,T$), maximum energy product ($336–352\,kJ\,m^{-3}$), and PSA intrinsic coercivity ($\approx1000\,kA\,m^{-1}$ at $50\,°C$)—closely match those of conventionally sintered samples.

FEM analysis reveals that the sample's maximum temperature during heating, crucial for final density, depends on the heating rate. For high heating rates, a few minutes of dwell time is required for the temperature to level off. Our study shows that the powder could be effectively densified within $\approx9\,min$. While fast ramping does not necessarily promote densification, it notably enhances the energy efficiency of the process. Increasing the heating rate from 10 to $200\,°C\,min^{-1}$ leads to a substantial reduction in energy consumption, from 6.34 to 2.56 MJ, representing approximately a 60% decrease. Comparative analysis with literature data reveals that RAS exhibits energy efficiency at least tenfold greater than slow conventional sintering methods.

Fast heat dissipation within the Nd–Fe–B material during heating effectively prevents microstructural inhomogeneities, namely, density and phase composition variations, in the final samples, as confirmed by SEM analysis and reflected in the high squareness of the demagnetization curves. Moreover, rapid heating in RAS was found not to hinder grain growth or notably affect the final microstructure, suggesting that high heating rates minimally alter the sintering mechanisms for the Nd–Fe–B system. In light of these findings, the reduction in dwell times is attributed to the highly efficient heat transfer facilitated by thermal radiation, underscoring the fundamental advantage of the RAS sintering strategy.

Conflict of Interest

The authors declare no conflict of interest.

Author Contributions

Tomaž Tomše: Conceptualization (lead); Investigation (lead); Methodology (equal); Writing—original draft (lead); Writing—review & editing (equal). **Aljaž Iveković**: Investigation (supporting); Methodology (equal); Writing—review & editing (supporting). **Andraž Kocjan**: Conceptualization (supporting); Methodology (equal); Writing—review & editing (equal). **Sašo Šturm**: Validation (equal); Writing—review & editing (equal). **Kristina Žužek**: Supervision (lead); Validation (equal); Writing—review & editing (equal).

Data Availability Statement

The data that support the findings of this study are available from the corresponding author upon reasonable request.

Keywords

[1] L. H. Lewis, F. Jiménez-Villacorta, *Metall. Mater. Trans. A* **2013**, *44*, 2.

[2] J. Bernardi, J. Fidler, M. Sagawa, Y. Hirose, *J. Appl. Phys.* **1998**, *83*, 6396.

[3] M. Zakotnik, C. O. Tudor, L. T. Peiró, P. Afiuny, R. Skomski, G. P. Hatch, *Environ. Technol. Innov.* **2016**, *5*, 117.

[4] C. Wang, W. Ping, Q. Bai, H. Cui, R. Hensleigh, R. Wang, A. H. Brozena, Z. Xu, J. Dai, Y. Pei, *Science* **2020**, *368*, 521.

[5] M. Cologna, B. Rashkova, R. Raj, *J. Am. Ceram. Soc.* **2010**, *93*, 3556.

[6] O. Guillon, J. Gonzalez-Julian, B. Dargatz, T. Kessel, G. Schierning, J. Räthel, M. Herrmann, *Adv. Funct. Mater.* **2014**, *16*, 830.

[7] D. S. B. Heidary, M. Lanagan, C. A. Randall, *J. Eur. Ceram. Soc.* **2018**, *38*, 1018.

[8] S.-J. L. Kang, in *Sintering: Densification, grain growth and microstructure*, Elsevier, Burlington, MA, USA **2005**.

[9] W. Ji, B. Parker, S. Falco, J. Zhang, Z. Fu, R. Todd, *J. Eur. Ceram. Soc.* **2017**, *37*, 2547.

[10] M. Y. Chu, M. N. Rahaman, L. C. De Jonghe, R. J. Brook, *J. Am. Ceram. Soc.* **1991**, *74*, 1217.

[11] A.-K. Hofer, A. Kocjan, R. Bermejo, *Addit. Manuf.* **2022**, *59*, 103141.

[12] T. Woodcock, Y. Zhang, G. Hrkac, G. Ciuta, N. Dempsey, T. Schrefl, O. Gutfleisch, D. Givord, *Scr. Mater.* **2012**, *67*, 536.

[13] T. Tomše, B. Podmiljšak, L. Scherf, R. Kessler, S. Kobe, A. Kocjan, S. Šturm, K. Žužek, *J. Mater. Process. Technol.* **2024**, *328*, 118405.

[14] D. Salamon, Z. Shen, P. Šajgalík, *J. Eur. Ceram. Soc.* **2007**, *27*, 2541.

[15] D. Salamon, K. Maca, Z. Shen, *Scr. Mater.* **2012**, *66*, 899.

[16] A. Kocjan, M. Logar, Z. Shen, *Sci. Rep.* **2017**, *7*, 2541.

[17] D. Li, Y. Liu, Y. Zhong, L. Liu, E. Adolfsson, Z. Shen, *Adv. Appl. Ceram.* **2019**, *118*, 23.

[18] D. Kuscer, A. Kocjan, M. Majcen, A. Meden, K. Radan, J. Kovač, B. Malič, *Ceram. Int.* **2019**, *45*, 10429.

[19] K. Sairam, J. Sonber, T. C. Murthy, A. Sahu, R. Bedse, J. Chakravartty, *Int. J. Refract. Hard Met.* **2016**, *58*, 165.

[20] D. Li, Z. Shen, *J. Eur. Ceram. Soc.* **2015**, *35*, 3303.

[21] D. Li, E. G. de Moraes, P. Guo, J. Zou, J. Zhang, P. Colombo, Z. Shen, *Sci. Technol. Adv. Mater.* **2014**, *15*, 045003.

[22] P. Cai, L. Guo, L. Liu, Q. Zhang, J. Li, Q. Lue, *Ceram. Int.* **2022**, *48*, 55.

[23] A. Kashimbetova, K. Slámečka, S. Díaz-de-la-Torre, J. C. Méndez-García, B. Hernández-Morales, M. C. Pina-Barba, D. Hui, L. Čelko, E. B. Montufar, *J. Mater. Res. Technol.* **2023**, *22*, 2147.

[24] Y. Matsuura, S. Hirosawa, H. Yamamoto, S. Fujimura, M. Sagawa, K. Osamura, *Jpn. J. Appl. Phys.* **1985**, *24*, L635.

[25] R. M. German, P. Suri, S. J. Park, *J. Mater. Sci.* **2009**, *44*, 1.

[26] S.-J. L. Kang, K.-H. Kim, D. N. Yoon, *J. Am. Ceram. Soc.* **1991**, *74*, 425.

[27] J. Svoboda, H. Riedel, R. Gaebel, *Acta Mater.* **1996**, *44*, 3215.

[28] A. J. Williams, P. J. McGuiness, I. R. Harris, *J. Less-Common Met.* **1991**, *171*, 149.

[29] C. Manière, A. Pavia, L. Durand, G. Chevallier, K. Afanga, C. Estournès, *J. Eur. Ceram. Soc.* **2016**, *36*, 741.

[30] F. Vial, F. Joly, E. Nevalainen, M. Sagawa, K. Hiraga, K. T. Park, *J. Magn. Magn. Mater.* **2002**, *242*, 1329.

[31] E. Perigo, H. Takiishi, C. Motta, R. Faria, *IEEE Trans. Magn.* **2009**, *45*, 4431.

[32] K. Uestuener, M. Katter, W. Rodewald, *IEEE Trans. Magn.* **2006**, *42*, 2897.

[33] J. Fischbacher, A. Kovacs, L. Exl, J. Kühnel, E. Mehofer, H. Sepehri-Amin, T. Ohkubo, K. Hono, T. Schrefl, *Scr. Mater.* **2018**, *154*, 253.

[34] P. J. McGuiness, A. J. Williams, I. R. Harris, E. Rozendaal, J. Ormerod, *IEEE Trans. Magn.* **1989**, *25*, 3773.

[35] T.-H. Kim, S.-R. Lee, M.-W. Lee, T.-S. Jang, J. W. Kim, Y. Do Kim, H.-J. Kim, *Acta Mater.* **2014**, *66* 12.

[36] W. Li, T. Ohkubo, K. Hono, M. Sagawa, *J. Magn. Magn. Mater.* **2009**, *321*, 1100.

[37] M. Sagawa, S. Hirosawa, K. Tokuhara, H. Yamamoto, S. Fujimura, Y. Tsubokawa, R. Shimizu, *J. Appl. Phys.* **1987**, *61*, 3559.

[38] L. Schultz, A. M. El-Aziz, G. Barkleit, K. Mummert, *Mater. Sci. Eng. A* **1999**, *267*, 307.

[39] M. F. Modest, in *Radiative Heat Transfer*, McGraw-Hill, Fayetteville, TX, USA **1993**.

[40] A. Nisar, C. Zhang, B. Boesl, A. Agarwal, *Ceramics* **2021**, *4*, 20.

[41] https://e-magnetsuk.com/introduction-to-neodymium-magnets/characteristics-of-ndfeb-magnets/ (accessed: April 2024).